BULLETIN OF THE POLISH ACADEMY OF SCIENCES
TECHNICAL SCIENCES, Vol. 67, No. 5, 2019
DOI: 10.24425/bpasts.2019.130882

Analysis on electromechanical coupling vibration characteristics of in-wheel motor in electric vehicles considering air gap eccentricity

Y. LI[1, 2]*, H. WU[3], X. XU[1], Y. CAI[1], and X. SUN[1]

[1] Automotive Engineering Research Institute, Jiangsu University, Zhenjiang, 212013, P. R. China
[2] Key Laboratory of Advanced Manufacture Technology for Automobile Parts (Chongqing University of Technology), Ministry of Education, Chongqing 400054, P. R. China
[3] School of Automotive and Traffic Engineering, Jiangsu University, Zhenjiang, 212013, P. R. China

Abstract. The distortion of air gap magnetic field caused by the rotor eccentricity contributes to the electromechanical coupling vibration of the brushless DC (BLDC) permanent magnet in-wheel motor (PMIWM) in electric vehicles (EV). The comfort of the BLDC in-wheel motor drive (IWMD) EV is seriously affected. To deeply investigate the electromechanical coupling vibration of the PMIWM under air gap eccentricity, the PMIWM, tyre and road excitation are analyzed first. The influence of air gap eccentricity on air gap magnetic density is investigated. The coupling law of the air gap and the unbalanced magnetic force (UMF) is studied. The coupling characteristics of eccentricity rate, air gap magnetic density, UMF, phase current and vibration acceleration are verified on the test bench in the laboratory. The mechanism of the electromechanical coupling vibration of the BLDC PMIWM under air gap static eccentricity (SE), dynamic eccentricity (DE) and hybrid eccentricity (HE) is revealed. DE and HE deteriorate the vibration acceleration amplitude, which contributes the electromechanical coupling vibration of the PMIWM. The research results provide a solid foundation for the vibration and noise suppression of the PMIWM in distributed drive EV.

Key words: BLDC in-wheel motor, rotor eccentricity, unbalanced magnetic force, electric vehicle, electromechanical coupling vibrat.

1. Introduction

With the increase of global automotive ownership, the energy crisis and environmental pollution have become essential factors that restrict the development of the automotive industry [1]. Electric vehicles with the characteristics of clean energy consuming and non-polluting are becoming the development trend of automotive in the future. The brushless DC (BLDC) in-wheel motor drive (IWMD) technology integrates the drive motor and the hub to simplify the vehicle powertrain system, increase the interior space and improve energy efficiency [2, 3]. Therefore, the IWMD electric vehicles (EV) improve the electrification level of modern vehicles. As an important part of the intelligent transportation system (ITS), electric vehicles (EV) are supposed to improve traffic safety and travel efficiency, and realize modern intelligent transportation. Electrification and intellectualization have become the development trend of future vehicles [4–6]. The research and development of IWMD EV that can guarantee the safety and low energy cost have become the goal pursued by most of the governments and automotive industries in the world.

As the power source of the IWMD EV, the IWMD system has the advantages of compact structure, high efficiency, energy saving and quick response. However, the employment of the in-wheel motor significantly increases the unsprung mass of the whole vehicle. The electromagnetic vibration of the in-wheel motor is directly delivered to the vehicle body through the wheels, resulting in comfort reduction of the vehicle [7–9]. In addition, the air gap eccentricity will be caused by unbalanced load, bearing friction, bearing bending, road surface excitation and other factors while the vehicle is operating. That also leads to further aggravation in torque ripple of the in-wheel motor, which seriously affects the comfort and safety of the IWMD EV [10–12].

Normally, air gap eccentricity can be classified as static eccentricity (SE) and dynamic eccentricity (DE). The SE with a constant air gap is caused by the ellipse of the stator core and incorrect mounting position of the stator or the rotor. Shaft bending, bearing wear, mechanical vibration in severe condition will lead to DE, in which the position of minimize air gap changes with the rotating rotor. The electromagnetic force (EMF) differences with positions due to the unbalanced air gap, which affects the air gap flux density and harmonic field inside the air gap [13–15]. That will lead to a change in cogging torque, motor performance and loss. 80% of rotor eccentricity is caused by mechanical assembly and 60% of the mechanical fault derives from air gap eccentricity [16]. In-wheel motor installed inside the wheel hub works in harsh environment with road excitation and vibration. SE, DE and hybrid eccentricity (HE) including both of SE and DE have significant influence on the performance of IWMD. Therefore, it is necessary to investigate the performance of the in-wheel motor with air gap eccentricity.

Many researchers have done research on air gap eccentricity of the motor. Deng et al. studied the influence on EMF of the

*e-mail: liyongthinkpad@outlook.com

Manuscript submitted 2019-05-03, revised 2019-06-21, initially accepted for publication 2019-07-11, published in October 2019

air gap eccentricity of PMSM [17]. Analytical method and finite element method (FEM) were used to analyze the influence of SE and DE eccentricity on electromagnetic force. It was concluded that the additional components of EMF and unbalanced magnetic force (UMF) were produced by SE and DE. It was also studied that the linear UMF components changed with eccentricity rate. In [18], the distribution of radial electromagnetic force under SE was studied. Since most of the eccentricity inside the motor is presented in the form of HE, there are still some errors between the actual mixed eccentricity and the static eccentricity or dynamic eccentricity. The changes and expression of air gap flux under HE eccentricity of induction motor was studied in [19]. The current and magnetic density harmonics produced under HE of the induction motor was investigated in [20]. The mathematical analytical expressions of SE, DE and HE of motor without any load were established in [21]. The EMF and UMF can be calculated from the air gap magnetic field. Li studied the air gap magnetic field and UMF of motor under different eccentricity [22]. It was concluded that the influence of stator eccentricity and rotor eccentricity on the unidirectional magnetic tension is different. The global analytical model of permanent magnet motor was established based on perturbation theory in [23]. The eccentricity air gap magnetic field distribution is obtained from the zero-order and the first-order component of the air gap magnetic density. The Maxwell tensor method was used to calculate the rotor unbalanced magnetic tension and cogging torque. The frequency distribution of radial EMF was analyzed based on the model of the air gap and radial EMF under rotor eccentricity in [24]. The transient distribution of the magnetic field of the air gap, Cogging Torque and UMF were calculated through magnetic conductivity function considering stator cogging and rotor eccentricity in [25]. The influence of rotor eccentricity on the performance of parallel winding permanent magnet synchronous motor (PMSM) is studied in [26]. It was found that the UMF caused by rotor eccentricity led to an increase in mechanical loss. The motor performance under rotor eccentricity was analyzed and evaluated based on the equivalent magnetic circuit model of PMSM. Luo et al. [27] analyzed the influence of UMF generated by the in-wheel motor on the lateral and vertical coupling dynamics of electric vehicles. It was concluded that the UMF should be necessarily considered in vehicle design to decrease the lateral and vertical coupling vibration.

Most of the current research focuses on the theoretical analysis of the rotor eccentricity, UMF and the vibration characteristics analysis of the outer rotor in-wheel motor independently [17–27]. Few researches were studied on the analysis of the electromechanical coupling vibration of the IWMD system. The electromechanical coupling model of IWMD system was established based on the electromagnetic torque model and vibration equation [28, 29]. The influence of electromechanical coupling vibration to the torque ripple and vibration characteristics was analyzed. The influence of electromechanical coupling to the longitudinal vibration of the IWMD system was investigated based on its dynamic model. However, the research on the mechanism of electromechanical coupling vibration under air gap eccentricity of IWMD is rare. The comfort of IWMD EV mainly depends on the outer rotor in-wheel motor. Therefore, it is necessary to study the mechanism of electromechanical coupling vibration of hub motor under air gap eccentricity.

The contribution of this paper is to present the electromechanical coupling vibration characteristics of outer rotor in-wheel motor considering air eccentricity through theoretical analysis and experimental investigation. The electromagnetic vibration characteristics and mechanism of IWMD system are revealed, which provides a solid theoretical and experimental foundation for vibration and noise suppression of the vehicle.

The paper is organized as follows. First, the dynamical model of permanent magnet in-wheel motor (PMIWM) is analyzed in Section 2. The EMF analysis under eccentricity, in Section 3, is presented. After that, in Section 4, the electromagnetic coupling vibration characteristics are analyzed. Section 5 is devoted to the conclusions and future work.

2. Electromechanical coupling model and analysis under air gap eccentricity

To build the accurate model of the in-wheel motor drive system, the electromechanical coupling under air gap eccentricity is analyzed firstly. The electromechanical coupling schematic under air gap eccentricity is shown in Fig. 1. The in-wheel motor, tyre and road excitation of electromechanical coupling vibration are modelled as follows, respectively.

2.1. Mathematical model of the PMIWM. To simplify the modelling analysis of the PMIWM, some assumptions are as following: (1) the motor cover effect is ignored. (2) the core permeability is infinity. (3) the magnetic permeability is equal to that of the air[30, 31].

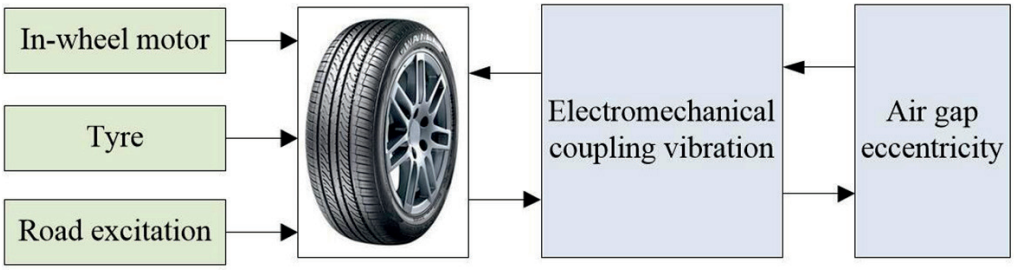

Fig. 1. The electromechanical coupling schematic under air gap eccentricity

The electromagnet torque of the PMIWM without air gap eccentricity is expressed as

$$T_e = \frac{(i_a e_a + i_b e_b + i_c e_c)}{\omega} \tag{1}$$

where i_a, i_b and i_c are the current of phase-a, phase-b and phase-c of the stator, respectively; e_a, e_b and e_c are the back EMF of phase-a, phase-b and phase-c of the stator, respectively; ω denotes the mechanical angular velocity of the PMIWM.

2.2. Tyre model. Tyre model is one of the most important parts of vehicle dynamics model, which bears the adhesion between vehicle and ground [32]. The semi-empirical model under longitudinal slip and lateral slip is used in this paper. Assume the lateral deformation only occurs on the tyre, and both of the rotation angle around x-axis and the displacement along z-axis are neglected.

In particular, S_x and S_y are introduced into the unified semi-empirical model as follows:

$$g = \begin{cases} S_x = (V_x - \omega r_t)/|V| \\ S_y = V_y \cos\alpha/|V| \\ V = \sqrt{V_x^2 + V_y^2} \end{cases} \tag{2}$$

where V is the tyre rotating speed, V_x, V_y are the tyre speed component on x-axis and y-axis, respectively; r_t is the radius of the rolling wheel; α is the sideslip angle between the tyre and the wheel rotating surface.

2.3. The model of excitation on the road surface. When the vehicle operates on the road, the time frequency power spectral density is expressed as [27, 33]

$$G_q(f) = G_q(n_0) n_0^2 \frac{V_v}{f^2} \tag{3}$$

where n_0 is the reference spatial frequency, $G_q(n_0)$ is the road roughness coefficient, f is the equivalent time frequency, V_v is the vehicle speed.

3. UMF analysis under air gap eccentricity

3.1. Air gap magnetic density. The air gap of the in-wheel motor with eccentricity is shown in Fig. 2.

As shown in Fig. 2, the length of the air gap of the surface mounted PMIWM changes with the time, which can be expressed as follows

$$\delta(\theta, t) = \delta_0 \left[1 - \varepsilon \cos(\omega_r t - \phi)\right] \tag{4}$$

where: δ is the length of the air gap of the rotor eccentricity, θ is the rotor angle, δ_0 is the average air gap length of the rotor without eccentricity, ε is the is the relative eccentricity, ϕ is the rotor angular position.

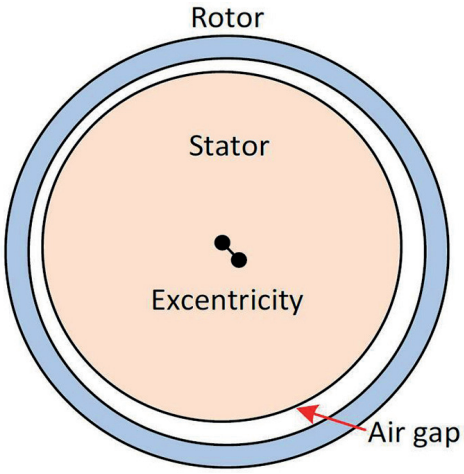

Fig. 2. Air gap of the in-wheel motor with eccentricity

The air gap magnetic flux can be expressed as

$$\Lambda(\theta, t) = \frac{\mu_a}{\delta(\theta, t)} = \sum_{n=0}^{\infty} \Lambda_n \cos n(\theta - \phi) \tag{5}$$

where μ_a is the coefficient of the magnetic flux of the air.

The magnetic field inside the air gap changes obviously with the air gap length when the rotor eccentricity occurs. The air gap magnetic field changes with the eccentricity rate. According to the solution of permanent magnet magnetic field, the armature winding magnetic field and air gap permeance, the air gap magnetic density of PMIWM can be obtained [35–37].The radial air gap magnetic field under eccentricity can be described as

$$\begin{aligned} B_r(\theta, t) = & \sum_{n}^{\infty} B_{pr} \cos(k_1\theta - k_2 t) + \\ & + \sum_{v} B_{ar} \cos(k_3\theta \pm \omega_r t) + \\ & + \sum_{n}^{\infty} B_{pr} \cos\left[(k_1 \pm 1)\theta - \left(k_2\theta \pm \frac{\omega_r}{p_n}\right)t\right] + \\ & + \sum_{v} B_{ar} \cos\left[(k_3 \pm 1)\theta \pm \left(\omega_r \pm \frac{\omega_r}{p_n}\right)t\right] \end{aligned} \tag{6}$$

where $B_{pr}(\theta, t)$ is the radial flux density of permanent magnet, $B_{ar}(\theta, t)$ is the radial flux density of magnetic field produced by the armature, k_1 is the spatial order of the magnetic field, k_2 is the angular frequency of the magnet field, k_3 is the spatial order of the armature winding, ω_r is the angular frequency of the armature winding, p_n is the pole pair number of the PMIWM, θ is the variable in polar coordinate.

The distribution of air gap magnetic density is not completely sinusoidal due to the motor cogging without air gap eccentricity. In this condition, it can be seen that the overall distribution of the air gap magnetic density of the motor is relatively uniform. However, the air gap magnetic density presents unevenly along the circumferential direction under air gap eccentricity [38, 39].

3.2. UMF modelling. The UMF is produced inside the air gap of the PMIWM under air gap eccentricity. That brings great influence to the performance of the motor, such as vibration and noise increasing, bearing wear and maintenance difficulty. To investigate the electromechanical coupling vibration mechanism of PMIWM, it is necessary to analyze the UMF [35, 40–42].

The radial force and the tangential force under air gap eccentricity can be obtained based on the Maxwell tensor. By decomposing the radial force and the tangential force on x-axis and y-axis, the UMF can be expressed as

$$f_x = \frac{r}{2\mu_0}\int_0^{2\pi}\Big[\Big(B_r^2(\theta,t) - B_t^2(\theta,t)\Big)\cos\theta + \\ + 2B_r(\theta,t)B_t(\theta,t)\sin\theta\Big]d\theta \tag{7}$$

where r is the UMF coefficient, μ_0 is the magnetic permeability of the air.

The 1-order radial force is used to judge the existence of UMF when the rotor eccentricity of the PMIWM occurs. The corresponding frequency of 1-order radial force is 0 Hz under SE, while the corresponding frequency of 1-order radial force is f/p_n under DE. f is the frequency of the three-phase current. Compared with the uniform air gap, high-order force is produced under air gap eccentricity, which leads to great electromagnetic vibration and noise.

3.3. Electromechanical coupling vibration under air gap eccentricity. The rotor eccentricity brings obviously influence to the air gap of PMIWM system, which changes the distribution of magnet density inside the air gap [43, 44]. There are some fluctuations in the output torque of the PMIWM caused by the non-uniform air gap, which leads to severe vibration and noise. The radial electromagnetic force generated by the air gap magnetic field excites the stator, rotor, winding, end cover and enclosure of the PMIWM [45, 46].

The resonance occurs when the frequency of the EMF approaches to the natural frequency of the PMIWM. The vibration acceleration of the stator caused by the rotor eccentricity can be expressed as follows without considering the motor cogging [47–49].

$$v_s = \frac{p_n r_i}{r_a\sqrt{2}\sqrt{1-\varepsilon^2}}\left(\frac{\omega_r r_a^2}{\omega_r^2 m_u r_a^2 - Gl_j}\right) \tag{8}$$

where r_i is the inner radius of the stator, r_a is the average radius of the stator yoke, m_u is the unit surface quality of the stator yoke, G is the elasticity modulus of the stator, l_j is the depth of the stator yoke.

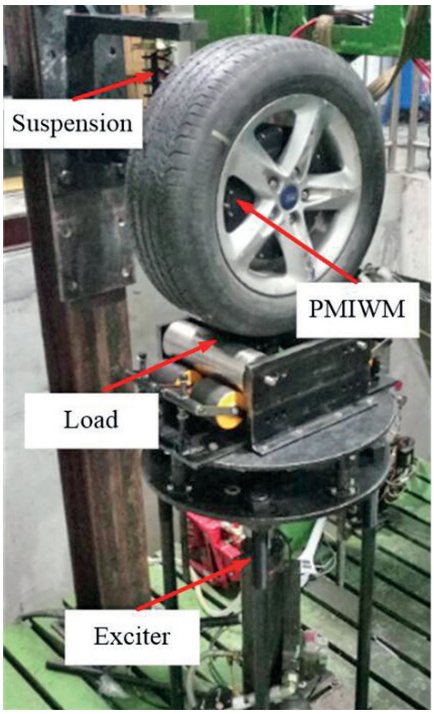

Fig. 3. PMIWM test bench

4. Electromechanical coupling vibration characteristics analysis

A novel PMIWM is developed in this study. The test bench shown in Fig. 3 is built to test the performance of the PMIWM. The parameters of the IWMD electric vehicle are illustrated in Table 1.

Table 1
Parameters of the in-wheel motor

Parameters	Value	Unit
Nominal power	8	kw
Nominal speed	1600	r/min
Slot number of stator	36	N/A
The outer diameter of the rotor	303	mm
The inner diameter of the rotor	283	mm
The outer diameter of the stator	273	mm
Magnet length	50	mm
Magnet width	24	mm
Magnet depth	4	mm
Slot width	11	mm
Wires number per slot	195	N/A
Motor length	107	mm
Air gap length	0.6	mm
Pole pair number	16	N/A

4.1. Eccentricity and magnetic density of the air gap. The corresponding disposition between the rotor and the stator, on one hand, is produced by the electromechanical coupling vibration of the PMIWM, which leads to the rotor eccentricity. On the other hand, the aberrance of the air gap magnet field has a great influence to the characteristics of the gap magnetic field and the coupling vibration of the PMIWM. The air gap magnetic density doesn't change with the time. That is caused by the non-uniform distribution of the air gap magnetic field. The magnetic density will increase when the length of air gap decreases. The magnetic density will decrease when the length of air gap increases. And, the aberrance of the magnetic density occurs inside the air gap.

The time response of the air gap magnetic density under SE, DE and HE, when the motor is operating at a speed of 300 r/min, are shown in Fig. 4a, Fig. 4b and Fig. 4c, respectively. From Fig. 4a, it can be seen that the air gap magnetic density under SE still changes periodically with the time. The air gap magnetic density changes by one period when the rotor passes a pair of magnetic poles. The reason is that the distribution of air gap magnetic field along the circumference does not change with time under SE. In the case of DE, in Fig. 4b, the air gap magnetic density no longer changes periodically during the rotation, and it is also distorted in time. This is because the DE makes the distribution of the entire air gap magnetic field change with time. The radial electromagnetic force magnetic density changes with time, and it no longer distributes unevenly along the circumference. We can see from Fig. 4c, the aberrance of the air gap magnetic density under HE is more severe than that under SE and DE shown in Fig. 4a and Fig. 4b, respectively.

The frequency response of the air gap magnetic density under SE, DE and HE are shown in Fig. 5a, Fig. 5b and Fig. 5c, respectively. It can be seen that the frequency distribution under SE, DE and HE condition are similar. Compared with the SE, both of DE and HE don't have obvious influence on the frequency distribution of air gap. Fig. 5a, Fig. 5b and Fig. 5c show that the main frequencies with large magnetic density are 16 Hz, 48 Hz, 240 Hz and 368 Hz, respectively, which are odd numbers of base-frequencies of the current. Compared with main frequencies under SE in Fig. 5a, it can be found that there are lots of harmonic components inside the red ellipses in Fig. 5b and Fig. 5c around 16 Hz, 48 Hz, 240 Hz and 368 Hz. The harmonic components around main frequencies in Fig. 5c are getting worse than that in Fig. 5b. From top to bottom in Fig. 5, we can also find that the amplitude of magnetic density is getting larger at 16 Hz, 48 Hz, 240 Hz and 368 Hz with the increasing eccentricity under SE, DE and HE, respectively.

To study the influence of air gap eccentricity rate on the amplitude of electromagnetic force, the fast Fourier transform (FFT) is used in the analysis of radial UMF under different eccentricity rates. The EMF order under SE, DE and HE is shown in Fig. 6. It can be seen that the EMF 1-order, 2-order and 3-order have large amplitude than other EMF order. Vibration and noise will be excited by the abovementioned EMF orders, which bring severe fluctuations to the PMIWM torque.

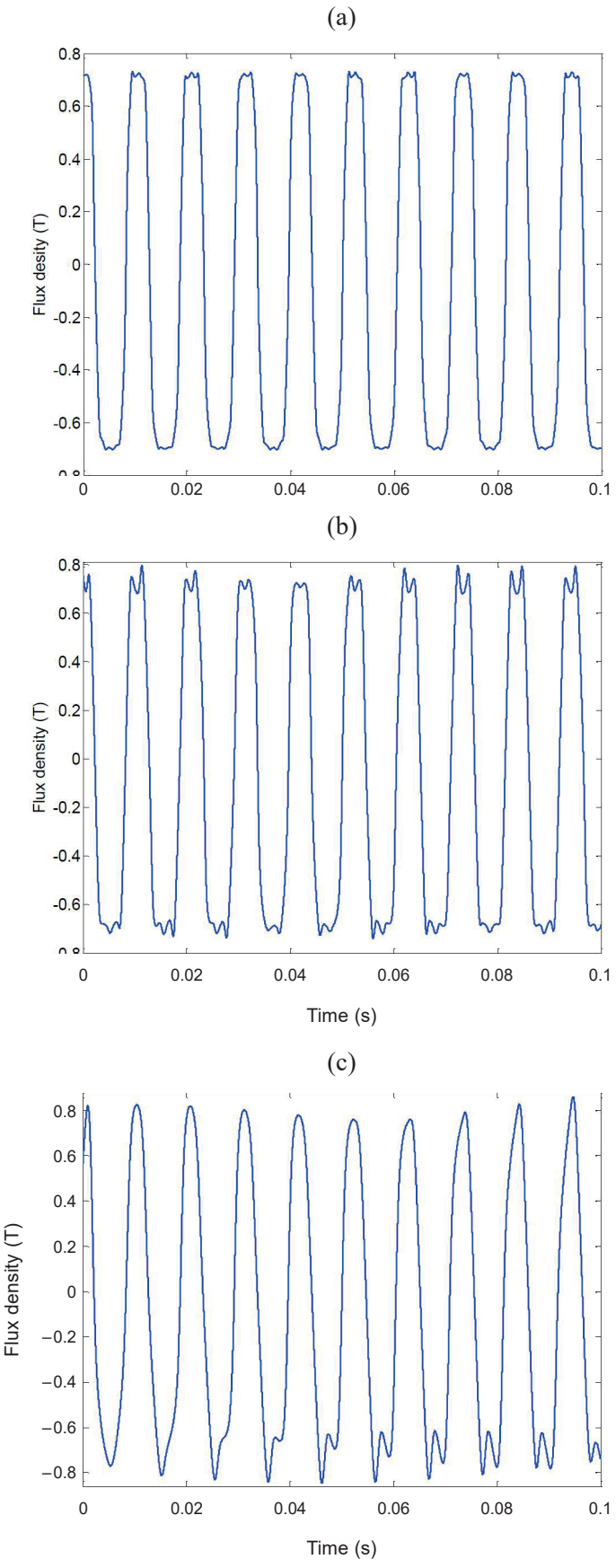

Fig. 4. Time response of air gap magnetic density at 300 r/min (a) SE, (b) DE, (c) HE

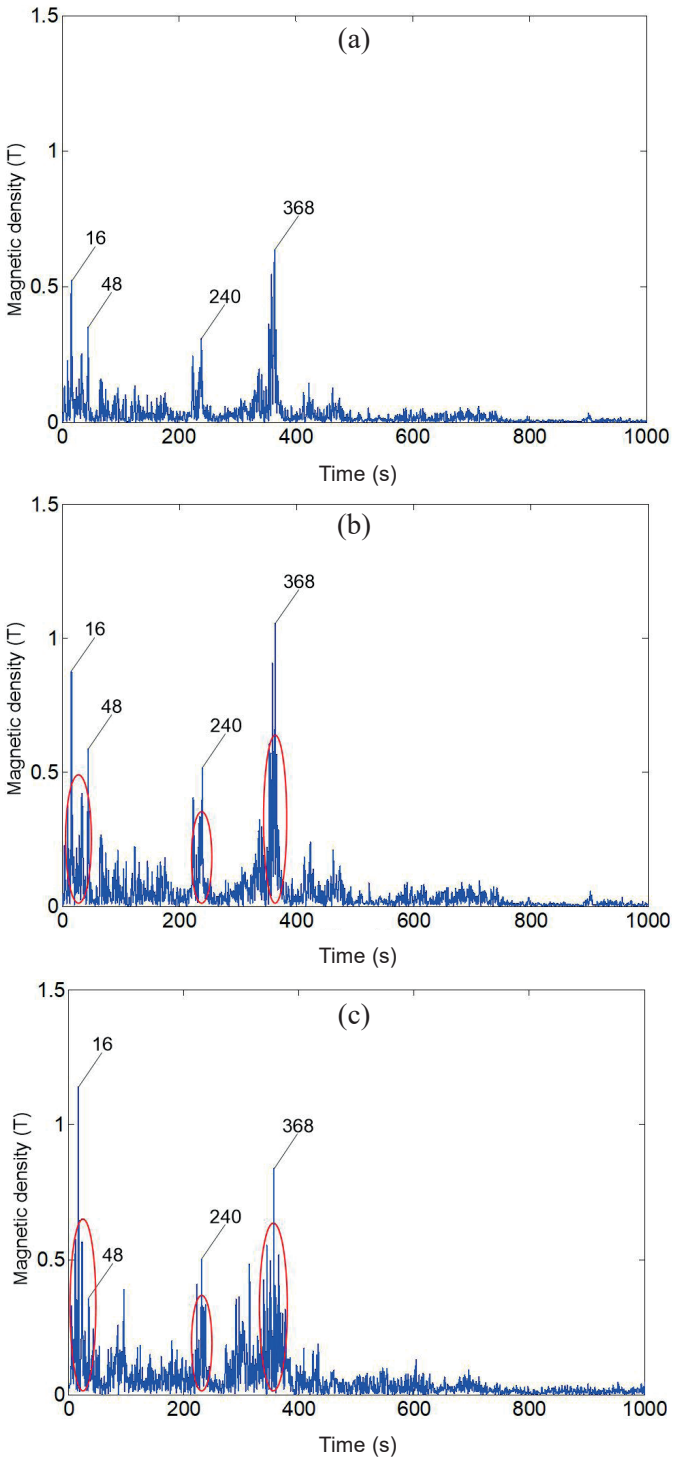

Fig. 5. Frequency response of air gap magnetic density at 300 r/min (a) SE, (b) DE, (c) HE

The relationship between the amplitude of radial UMF and the eccentricity rate is shown in Fig. 7, which shows the relationship between the EMF generated by the air gap eccentricity and the eccentricity rate. It can be concluded that the EMF caused by the air gap eccentricity increases linearly with the eccentricity rate. The magnetic permeability of the permanent magnet and that of the air gap are close to each other due to

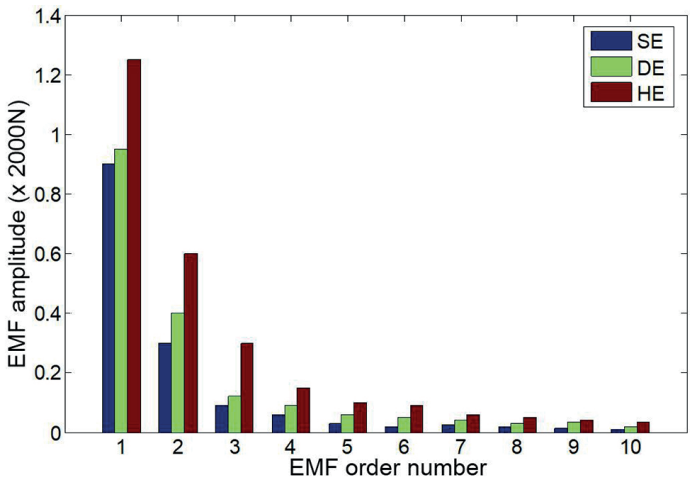

Fig. 6. The EMF order diagram

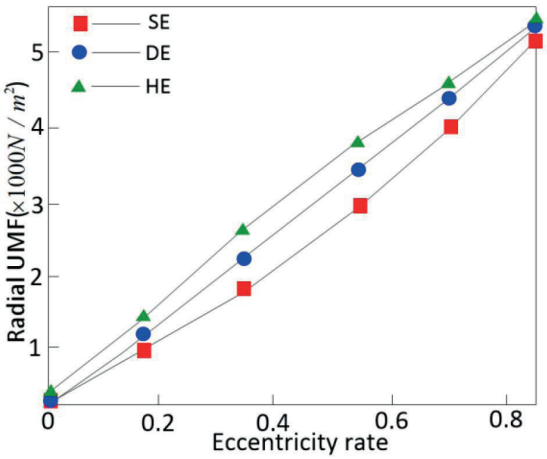

Fig. 7. The curve of UMF vs. eccentricity rate

the thickness of the permanent magnet of the PMIWM. That leads to a small effective eccentricity rate and linear amplitude of the force wave order under eccentricity. The frequency and the amplitude of the radial EMF are influenced by SE, DE and HE. The amplitude of the radial EMF changes linearly with the increase of the eccentricity rate.

4.2. Eccentricity and phase current. To study the relationship between the eccentricity and the phase current, the phase-a current under different rotor eccentricity rate at a speed of 300 r/min and a constant load of 20 Nm is analyzed. The phase-a current under SE is shown in Fig. 8. It can be seen that, in Fig. 8a, the time response of phase-a current under different SE rate 0, 0.2, 0.4, 0.6 and 0.8 are shown from top to bottom, respectively. Also, the current spectrum under different SE rate 0, 0.2, 0.4, 0.6 and 0.8 are shown in Fig. 8b, respectively. It can be seen that the amplitude of the low frequency of the current under different SE rates is much larger than that of the high frequency of the current. The phase-a current under DE is shown in Fig. 9. It can be seen that, in Fig. 9a, the time response of

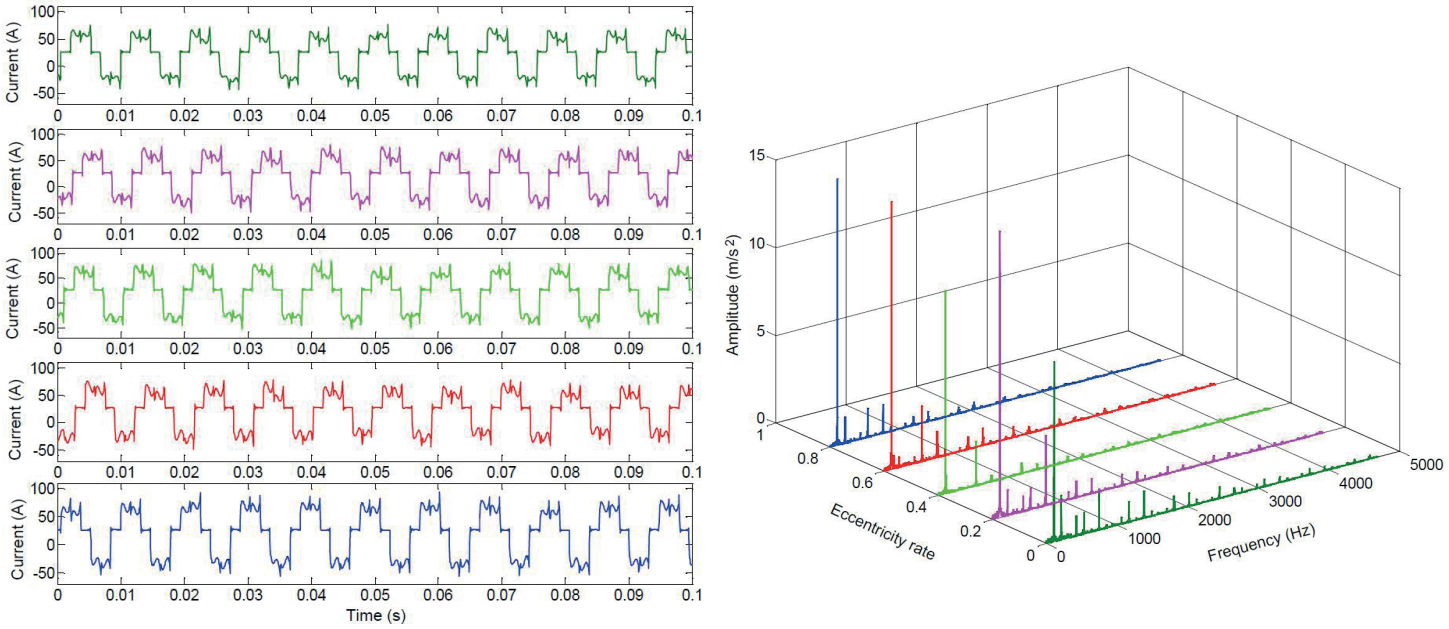

Fig. 8. Phase-a current under SE; (a) time response (b) frequency response

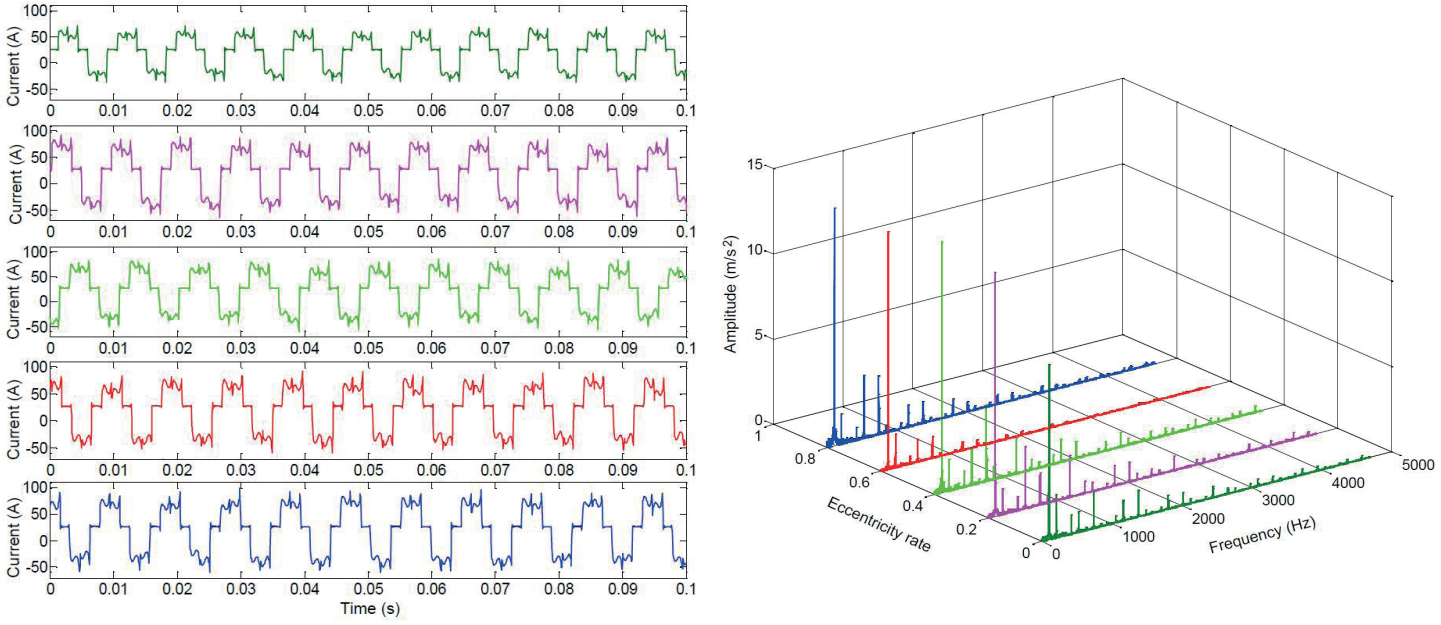

Fig. 9. Spectrum of phase-a current under DE, (a) time response, (b) frequency response

phase-a current under different DE rate 0, 0.2, 0.4, 0.6 and 0.8 are shown from top to bottom, respectively. Also, the current spectrum under different DE rate 0, 0.2, 0.4, 0.6 and 0.8 are shown in Fig. 9b, respectively. It can be seen that the amplitude of the low frequency of the current under different DE rates are becoming smaller when the current frequency is increasing. The phase-a current under HE is shown in Fig. 10. It can be seen that, in Fig. 10a, the time response of phase-a current under different HE rate 0, 0.2, 0.4, 0.6 and 0.8 are shown from top to bottom, respectively. The current spectrum under different HE rate 0, 0.2, 0.4, 0.6 and 0.8 are shown in Fig. 10b, respectively. It can be seen that the amplitude of the low frequency of the current under different HE retes are much larger than that of the high frequency. Especially at HE rate 0.8, the frequency amplitude of the current is larger than that under SE rate 0.8 and DE rate 0.8.

From Fig. 8a, Fig. 9a and Fig. 10a it can be seen the average amplitude of phase-a current increases with the air gap eccentricity rate. In the case of eccentricity rate 0.6, the maximum current amplitude is 78.6 A under SE, 92.9 A under DE

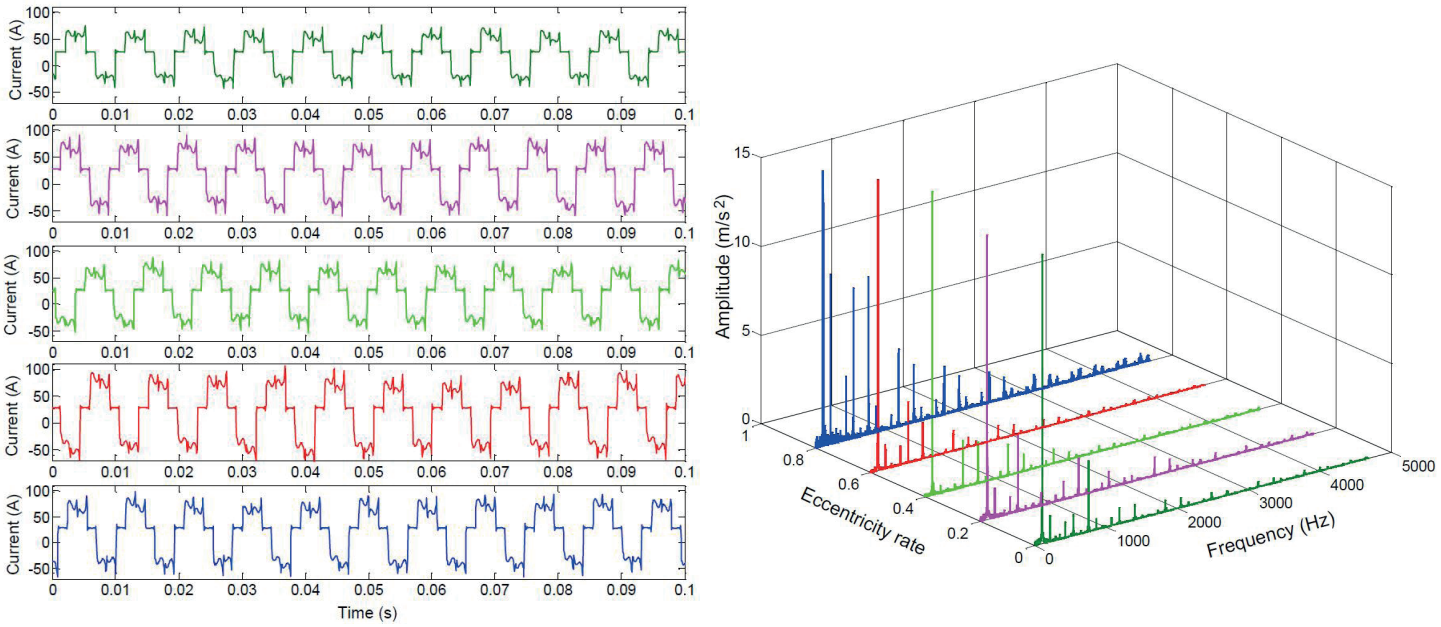

Fig. 10. Spectrum of phase-a current under HE; (a) time response, (b) frequency response

Table 2
Phase-a current fluctuation under eccentricity

Eccentricity rate	Maximum phase current (A)			Fluctuation coefficient (%)	
	SE	DE	HE	SE vs. DE	SE vs. HE
0.6	78.6	92.9	107.3	18.1	36.5

and 107.3 A under HE, respectively. Current fluctuation under different eccentricity rate is clearly shown in Table 2, which indicates the rotor eccentricity rate has a certain influence on phase current of PMIWM.

In Fig. 8b, Fig. 9b and Fig. 10b, from the current frequency response under different eccentricity rate, we can see the current has larger amplitude at low frequencies. There are much more harmonic components under eccentricity rate 0.8 in Fig. 10b than that under the same eccentricity rate in Fig. 8b and Fig. 9b. It also can be seen, from Fig. 8b, Fig. 9b and Fig. 10b, current amplitude just has influence on the electromechanical coupling vibration of the PMIWM. The frequency distribution is not affected by the current amplitude.

4.3. Eccentricity and vibration. The vibration acceleration caused by the rotor eccentricity is investigated in this section. The spectrum of the vibration acceleration under different SE rate 0, 0.2, 0.4, 0.6 and 0.8 on *x*-axis and *y*-axis are shown in Fig. 11, respectively. It can be seen from Fig. 11 the amplitude of the vibration acceleration increases with SE rate. The aver-

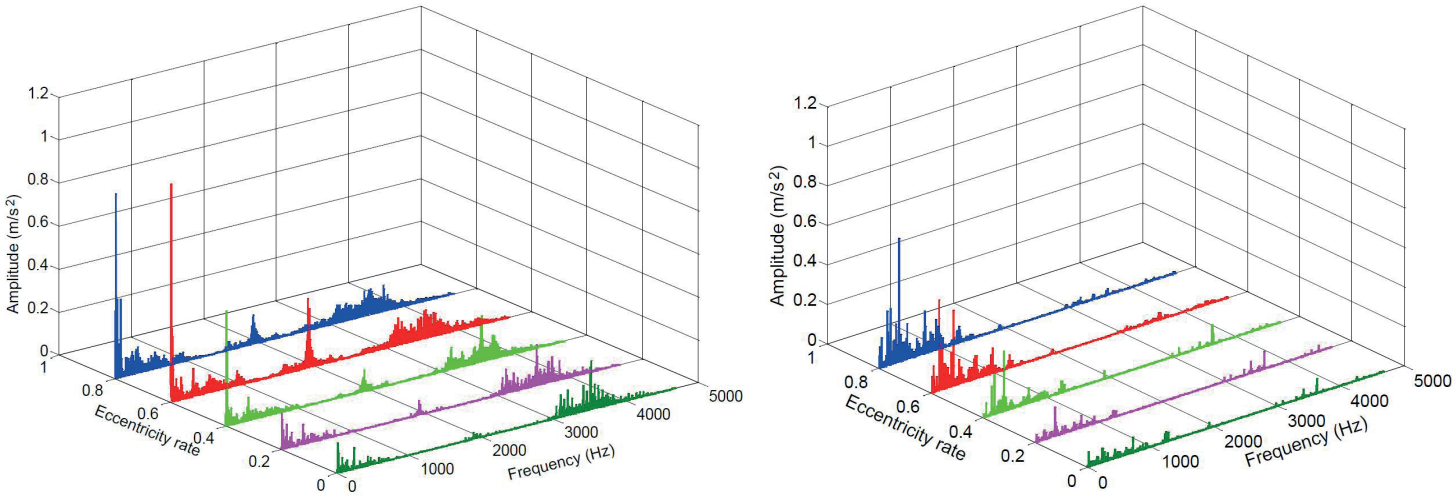

Fig. 11. The spectrum of vibration acceleration under SE. (a) *x*-axis, (b) *y*-axis

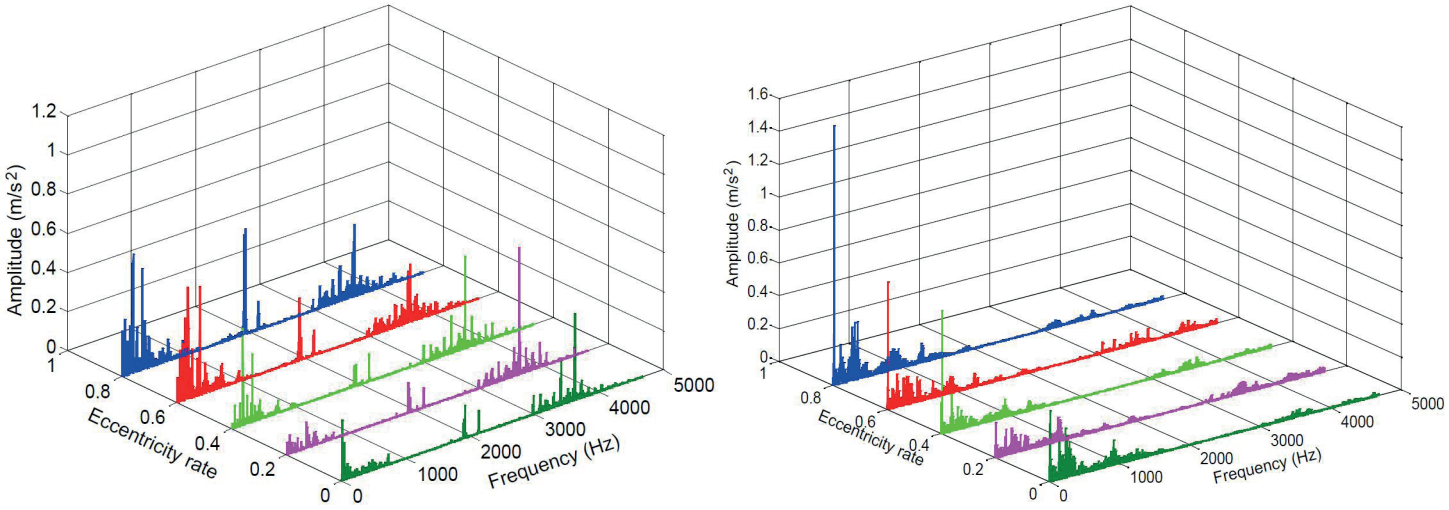

Fig. 12. Spectrum of vibration acceleration under DE. (a) *x*-axis, (b) *y*-axis

age amplitude of the vibration acceleration on *x*-axis is larger than that on *y*-axis. Compared with the amplitude of the vibration acceleration on *y*-axis, there are a lot of high frequency components than that on *x*-axis. The spectrum of the vibration acceleration under different DE rate 0, 0.2, 0.4, 0.6 and 0.8 on *x*-axis and *y*-axis are shown in Fig. 12, respectively. From Fig. 12 we can see the amplitude of the vibration acceleration also increases with the DE rate. The average amplitude of the vibration acceleration on *x*-axis is larger than that on *y*-axis. Compared with the amplitude of the vibration acceleration on *y*-axis, there are a lot of high frequency components than that on the *x*-axis. The main components of additional frequency change with the eccentricity rate. Whether it is SE or DE, the amplitudes of the vibration acceleration in large frequency range are obviously different. The main harmonic components under SE and DE can be clearly seen from Fig. 11and Fig. 12. It can be seen 350 Hz, 1900 Hz, 3200 Hz, 3500 Hz and 3700 Hz are main vibration frequency on *x*-axis under SE and DE. It also can be seen 10 Hz, 350 Hz, 500 Hz, 1100 Hz and 2000 Hz are main vibration frequency on *y*-axis under SE and DE.

To further study the influence of HE on electromechanical coupling vibration, HE testing is investigated based on the SE and DE experiment. The air gap magnet density changes with the time and rotor position angle under HE, during which both of SE and DE exist. The spectrum of the vibration acceleration under different HE rate 0, 0.2, 0.4, 0.6 and 0.8 on *x*-axis and *y*-axis are shown in Fig. 13, respectively

It can be seen from Fig. 13 the vibration acceleration amplitude increases with HE rate. The average amplitude of the vibration acceleration on *x*-axis is larger than that on *y*-axis. Compared with the vibration acceleration amplitude on *y*-axis, lots of high frequency components exist on *x*-axis. The main components of additional frequency change with the eccentric-

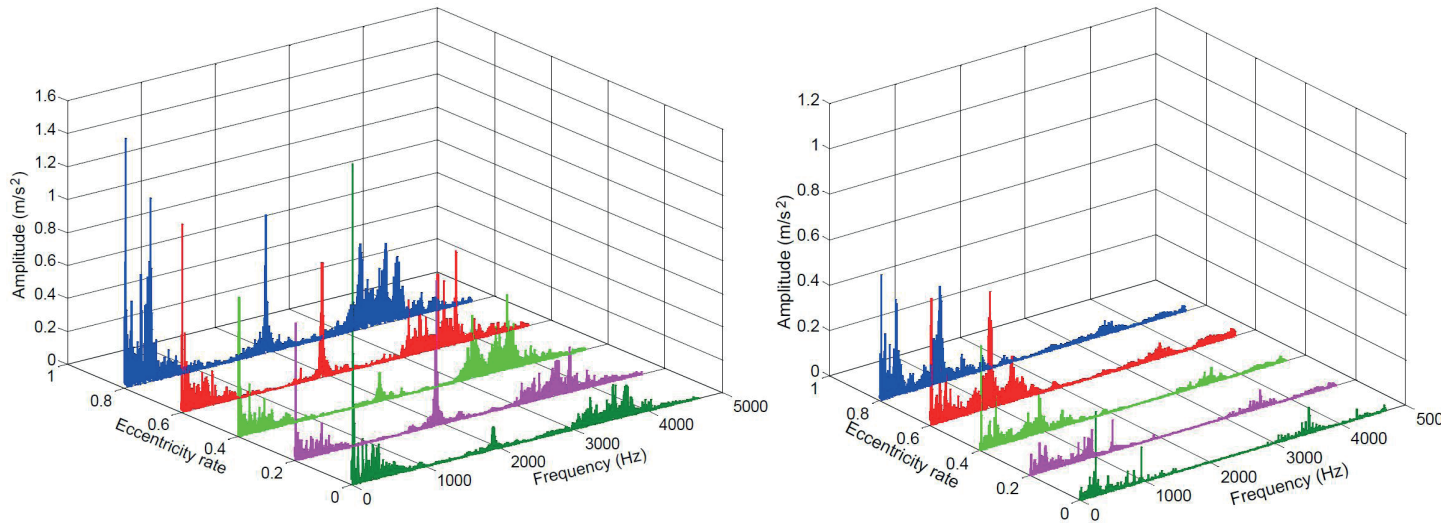

Fig. 13. The spectrum of vibration acceleration under HE. (a) *x*-axis, (b) *y*-axis

Table 3
Vibration amplitude under different eccentricity

Eccentricity rate		Frequency (Hz)	Acceleration amplitude (SE)	Acceleration amplitude (DE)	Acceleration amplitude (HE)	Deterioration	
						SE vs. DE (%)	SE vs. HE (%)
x-axis	0.2	500	0.04	0.08	0.16	100	300
	0.6	3600	0.1	0.21	0.43	110	330
y-axis	0.4	1000	0.01	0.08	0.18	700	1700
	0.8	800	0.07	0.11	0.21	57	200

ity rate. Compared with the single SE or the DE, the amplitudes of the vibration frequency are larger on both *x*-axis and *y*-axis.

To clearly show the deterioration brought by vibration acceleration under different eccentricity rate, the vibration acceleration amplitudes caused by the radial EMF of the PMIWM on both *x*-axis and *y*-axis under different eccentricities are analyzed and shown in Table 3. From Table 3, it can be seen the deterioration caused by DE under eccentricity rate 0.2 at 500 Hz and eccentricity rate 0.6 at 3600 Hz on *x*-axis are 100% and 110%, respectively. The deterioration caused by HE under the abovementioned condition is 300% and 330%, respectively. The deterioration caused by DE under eccentricity rate 0.4 at 1000 Hz and eccentricity rate 0.8 at 800 Hz on *y*-axis are 700% and 57%, respectively. The deterioration caused by HE under the abovementioned condition is 1700% and 200%, respectively. It can be concluded the vibration acceleration amplitude under DE and HE are much larger than that under SE. DE and HE deteriorate the vibration acceleration amplitude, which contributes the electromechanical coupling vibration of PMIWM.

5. Conclusions

The electromechanical coupling model of the PMIWM in distributed drive EV is established in this paper. The coupling rule between the air gap magnetic density and the UMF of the PMIWM is analyzed. The electromechanical coupling vibration mechanism caused by the air gap eccentricity is revealed. The following conclusions are shown as follows.

1) The distribution of the radial air gap magnetic density under SE and DE is uneven due to the uneven spatial distribution of the air gap magnetic field inside the PMIWM. The performance of the motor is affected. There are some fluctuations in the output torque of the motor, which lead to great vibration and noise. Compared with SE and DE, the distortion of the air gap magnetic density under HE is severe.
2) The amplitudes of the radial UMF under SE, DE and HE increase with the eccentricity rate. The influence of UMF on rotor vibration increases with the eccentricity rate under SE, DE and HE.
3) SE has the minor influence to the electromechanical coupling vibration. The vibration acceleration amplitude under DE and HE are much larger than that under SE. DE and HE deteriorate the vibration acceleration amplitude, which contributes the electromechanical coupling vibration of the PMIWM.

Future work will focus on the vibration and noise suppression of the IWMD system in EV.

Acknowledgements. This work was supported by the National Natural Science Foundation of China (51705213, U1664258), the Natural Science Foundation of Jiangsu Province (BK20160525), the Primary Research & Development Plan of Jiangsu Province (BE2017129) and the Key Laboratory of Advanced Manufacture Technology for Automobile Parts (2018KLMT05).

References

[1] M. Ehsani, Y. Gao, and A. Emadi, "Modern Electric, Hybrid Electric, and Fuel Cell Vehicles-Fundamentals. Theory and Design. Second Edition", *US:CRC Press* (2010).
[2] Y. Huang, H. Wang, and A. Khajepour, "A review of component sizing and power management strategy of Hybrid vehicles", *Renewable and sustainable energy review* 96, 132–144 (2018).
[3] Y. Li, B. Zhang, and X. Xu, "Decoupling control for permanent magnet in-wheel motor using internal model control based on back propagation neural network inverse system", *Bull. Pol. Ac.: Tech.* 66(6), 1–12 (2018).
[4] Q. Song, H. Wan, Y. Mi, and S. Ye, "Optimum control strategy of drive torque for pure electric vehicles during acceleration", *Journal of Jiangsu University (Natural Science Edition)* 38(1), 1–6 (2017).
[5] Y. Huang, S. Fard, M. Khazraee, and M. Khazraee, "An adaptive model predictive controller for a novel battery-powered anti-idling system of service vehicles", *Energy* 127, 318–327 (2017).
[6] H. Jiang, C. Li, Ma, S. S. Ding, and C. Zhang, "Path tracking control of automatic parking for intelligent vehicle based on non-smooth control strategy", *Journal of Jiangsu University (Natural Science Edition)* 38(5), 497–502 (2017).
[7] X. Sun, Y. Cai, C. Yuan, S. Wang, and L. Chen, "Fuzzy sliding mode control for the vehicle height and leveling adjustment system of an electronic air suspension", *Chinese Journal of Mechanical Engineering* 31(25), 1–13 (2018).
[8] H. Kang, Y. Son, and G. Kim, "The Noise and Vibration Analysis of BLDC Motor Due to Asymmetrical Permanent-Magnet Overhang Effects", *IEEE Transactions on Industry Applications*, 44(5) 1569–1577 (2018).
[9] Y. Huang, A. Khajepour, T. Zhu, and H. Ging, "A supervisory energy-saving controller for a novel anti-idling system of service vehicles", *IEEE/ASME Transactions on Mechatronics* 22(2),1037–1046 (2017).

[10] T. Chen, X. Xu, L. Chen, H. Jiang, Y. Cai, and Y. Li, "Estimation of longitudinal force, lateral vehicle speed and yaw rate for four-wheel independent driven electric vehicles", *Mechanical Systems and Signal Processing* 101(2), 377–388 (2018).

[11] Y. Li, H. Deng, X. Xu, and W. Wang, "Modelling and testing of in-wheel motor drive intelligent electric vehicles based on co-simulation with Carsim/Simulink", *IET Intelligent Transport Systems* 13(1),115–123 (2019).

[12] C. Yin, J. Zhang, and S. Wang, Influence of damper indicator diagram area on vehicle ride comfort", *Journal of Jiangsu University (Natural Science Edition)* 38(6), 645–651 (2017).

[13] Z. Liu, J. Huang, and S. He, "Diagnosis of air-gap eccentricity and partial demagnetisation of an interior permanent magnet synchronous motor based on inverse transient complex inductance vector theory", *IET Electric Power Applications* 12(8), 1166–1175 (2018).

[14] S. Mohamed, J. Antonio, C. Marques, Y. Khaled, and G. Adel, "The Use of the Modified Pronys Method for Rotor Speed Estimation in Squirrel-Cage Induction Motors", *IEEE Transactions on Industry Applications* 52(3), 2194–2202 (2016).

[15] X. Diao and H. Zhu, "Survey of decoupling control strategies for bearingless synchronous reluctance motor", *Journal of Jiangsu University (Natural Science Edition)* 38(6), 687–695 (2017).

[16] N. Elkasabgy, A. Eastman, and G. Dawson, "Detection of broker bar in the cage rotor on an induction machine", IEEE Transactions on Industry Applications 28(1), 165–171 (1992).

[17] W. Deng, S. Zuo, F. Lin, S. Wu, and Y. Mao, "Modeling and Analysis of Unbalanced Moment for an Axial-Flux in-Wheel Motor with Eccentricity", Transactions of China Electrotechnical Society 32(13),153–161 (2017).

[18] O. Oladapo and S. Paul, "Barendse, M.A.K. Influence of Rotor Topologies and Cogging Torque Minimization Techniques in the Detection of Static Eccentricities in Axial-Flux Permanent-Magnet Machine", *IEEE Transactions on Industry Applications* 53(1), 161–170 (2017).

[19] O. Mansour and M. Maryam, "Unified Modeling Technique for Axially Uniform and Nonuniform Eccentricity Faults in Three-Phase Squirrel Cage Induction Motors", *IEEE Transactions on Industrial Electronics* 65(7), 5292–5301 (2018).

[20] A. Rahideh and T. Korakianitis, "Analytical Open-Circuit Magnetic Field Distribution of Slotless Brushless Permanent-Magnet Machines With Rotor Eccentricity", *IEEE Transactions on Magnetics* 47(12), 4791–4808 (2011).

[21] P. Jun-Kyu and H. Jin, "Detection of Inter-Turn and Dynamic Eccentricity Faults Using Stator Current Frequency Pattern in IPM-Type BLDC Motors", *IEEE Transactions on Industrial Electronics* 63(3), 1771–1780 (2016).

[22] Y. Li and Z. Zhu, "Cogging Torque and Unbalanced Magnetic Force Prediction in PM Machines With Axial-Varying Eccentricity by Superposition Method", *IEEE Transactions on Magnetics* 53(11), 1–4(2017).

[23] T. Samad, J. Pezhman, and B. Nicola, "Analytical Modeling of No-Load Eccentric Slotted Surface-Mounted PM Machines, Cogging Torque and Radial Force", *IEEE Transactions on Magnetics* 53(12), 1–1 (2017).

[24] J. Song, K. Kang, C. Kang, and G. Jang, "Cogging Torque and Unbalanced Magnetic Pull Due to Simultaneous Existence of Dynamic and Static Eccentricities and Uneven Magnetization in Permanent Magnet Motors", *IEEE Transactions on Magnetics* 53(3),1–9 (2017).

[25] X. Sun, Y. Shen, S. Wang, G. Lei, Z. Yang, and S. Han, "Core losses analysis of a novel 16/10 segmented rotor switched reluctance BSG motor for HEVs using nonlinear lumped parameter equivalent circuit model", *IEEE/ASME Transactions on Mechatronics* 23(2), 747–757 (2018).

[26] Y. Li, Q. Lu, Z. Zhu, D. Wu, and G. Li, "Superposition Method for Cogging Torque Prediction in Permanent Magnet Machines With Rotor Eccentricity", *IEEE Transactions on Magnetics* 52(6), 1–1 (2016).

[27] Y. Luo and D. Tan, "Study on the Dynamics of the In-Wheel Motor System", *IEEE Transactions on Vehicular Technology* 61(8), 3510–3518 (2012).

[28] Y. Mao, S. Zuo, and F. Lin, "Lector mechanical coupled vibration characteristics of electric wheel under torque ripple", *Journal of Jilin University (Engineering and Technology Edition)* 47(03), 908–916 (2017).

[29] S. Zuo, D. Li, Y. Mao, W. Deng, and X. Wu, "Modeling and validation on longitudinal vibration characteristics of electric wheel system considering electromechanical coupling", *Transactions of the Chinese Society of Agricultural Engineering* 33(22), 61–68 (2017).

[30] Y. Li, B. Zhang, and X. Xu, "Robust control for permanent magnet in-wheel motor in electric vehicles using adaptive fuzzy neural network with inverse system decoupling", *Transactions of the Canadian Society for Mechanical Engineering* 42(3), 286–297 (2018).

[31] C. Li and L. Wu, "Sliding mode control for synchronization of fractional permanent magnet synchronous motors with finite time", *Optik-International Journal for Light and Electron Optics* 127(6), 3329–3332 (2016).

[32] H. Guo, Z. Yin, D. Cao, H. Chen, and C. Lv, "A Review of Estimation for Vehicle Tire-Road Interactions Toward Automated Driving", IEEE Transactions on Systems Man & Cybernetics Systems 49(1), 14–30 (2018).

[33] L. Zhang and H. Wang, "Shear stress analysis of asphalt pavement based on transverse contact stress", *Journal of Jiangsu University (Natural Science Edition)* 39(02), 236–241 (2018).

[34] B. Xu, C. Xiang, Y. Qin, P. Ding, and M. Dong, "Semi-Active Vibration Control for in-Wheel Switched Reluctance Motor Driven Electric Vehicle With Dynamic Vibration Absorbing Structures, Concept and Validation", *IEEE Journals & Magazines* 6, 60274–60285 (2018).

[35] S. Zuo, L. Gao, X. Wu C. Ma, and J. Shen, "The analysis of electromagnetic force in permanent magnet synchronous motors with rotor eccentricity in electric vehicles", *Journal of Jiamusi University* 32(02), 166–170 (2014).

[36] C. Ma, S. Zuo, L. He, S. Meng, and Q. Sun, "Analytical Model of permanent Magnet synchronous Motor considering slot and high order harmonics. Journal of Vibration", *Measurement and Diagnosis* 35(02), 231–237 (2015).

[37] X. Zhu, Z. Xiang, C. Zhang, L. Quan, Y. Du, and W. Gu, "Co-Reduction of Torque Ripple for Outer Rotor Flux-Switching PM Motor Using Systematic Multi-Level Design and Control Schemes", *IEEE Transactions on Industrial Electronics* 64(2), 1102–1112 (2018).

[38] J. Zhu, S. Li, D. Song, Q. Han, and G. Li, "Performance parameter analysis of a low speed AFPMSG with stator coreless", *Journal of Jiangsu University (Natural Science Edition)* 39(04), 445–452 (2018).

[39] X. Zhu, Z. Shu, L. Quan, Z. Xiang, and X. Pan, "Design and Multicondition Comparison of Two Outer-Rotor Flux-Switching Permanent-Magnet Motors for In-Wheel Traction Applications", *IEEE Transactions on Industrial Electronics* 64(8), 6137–6148 (2017).

[40] C. Ma, S. Zuo, S. Meng, and Q. Sun, "Analytical Calculation of Electromagnetic Torque in Permanent Magnet Synchronous Motor for Electric Vehicles", *Journal of Vibration, Measurement and Diagnosis* 32(05),756–761 (2012).

[41] Y. Zhou and Z. Zhu, "Torque Density and Magnet Usage Efficiency Enhancement of Sandwiched Switched Flux Permanent Magnet Machines Using V-Shaped Magnets", *IEEE Transactions on Magnetics* 49(7), 3834–3837 (2013).

[42] K. Kang, J. Song, C. Kang, S. Sung, and G. Jang, "Real-Time Detection of the Dynamic Eccentricity in Permanent-Magnet Synchronous Motors by Monitoring Speed and Back EMF Induced in an Additional Winding", *IEEE Transactions on Industrial Electronics* 64(9), 7191–7200 (2017).

[43] X. Tang, X. Hu, W. Yang, and H. Yu. "Novel Torsional Vibration Modeling and Assessment of a Power-Split Hybrid Electric Vehicle Equipped with a Dual Mass Flywheel", *IEEE Transactions on Vehicular Technology* 67,1990–2000 (2018).

[44] J. Wen, C. Song, Y. Fu, and P. Guo, "Rotor structure optimization of permanent magnet synchronous generator built-in type U", *Journal of Jiangsu University(Natural Science Edition)* 39(02), 194–198 (2018).

[45] Z. Song, Y. Yu, F. Chai, and Y. Tang, "Radial Force and Vibration Calculation for Modular Permanent Magnet Synchronous Machine With Symmetrical and Asymmetrical Open-Circuit Faults", *IEEE Transactions on Magnetics* 54(11), 1–5 (2018).

[46] T. Ishikawa, M. Yamada, and N. Kurita, "Design of Magnet Arrangement in Interior Permanent Magnet Synchronous Motor by Response Surface Methodology in Consideration of Torque and Vibration", *IEEE Transactions on Magnetics* 47(5), 1290–1293 (2011).

[47] M. Tsuda, T. Kojima, T. Yagai, and T. Hamajima, "Vibration Characteristics in Magnetic Levitation Type Seismic Isolation Device Composed of Multiple HTS Bulks and Permanent Magnets", *IEEE Transactions on Applied Superconductivity* 17(2), 2059–2062 (2007).

[48] F. Wang, X. Xu, Z. Fang, and L. Chen, "Study of the influence mechanism of pitch deviation on cylindrical helical gear meshing stiffness and vibration noise", *Automotive Engineering Research Institute* 9(9), 1–9 (2017).

[49] R. Tang, Z. Song, S. Yu, X. Hao, and W. Wang, "Study on source of vibration and acoustic noise of permanent magnet machines by inverter", *Electric Machines and Control* 14(03), 12–17 (2010).